



HAL
open science

Experimental and Theoretical Investigations of Low-Dimensional BiFeO₃ System for Photocatalytic Applications

Manal Benyoussef, Sébastien Saitzek, Nitul Rajput, Matthieu Courty,
Mimoun El Marssi, Mustapha Jouiad

► **To cite this version:**

Manal Benyoussef, Sébastien Saitzek, Nitul Rajput, Matthieu Courty, Mimoun El Marssi, et al..
Experimental and Theoretical Investigations of Low-Dimensional BiFeO₃ System for Photocatalytic
Applications. *Catalysts*, 2022, 12 (2), pp.215. 10.3390/catal12020215 . hal-03592621

HAL Id: hal-03592621

<https://hal.science/hal-03592621>

Submitted on 25 Aug 2023

HAL is a multi-disciplinary open access archive for the deposit and dissemination of scientific research documents, whether they are published or not. The documents may come from teaching and research institutions in France or abroad, or from public or private research centers.




L'archive ouverte pluridisciplinaire **HAL**, est destinée au dépôt et à la diffusion de documents scientifiques de niveau recherche, publiés ou non, émanant des établissements d'enseignement et de recherche français ou étrangers, des laboratoires publics ou privés.



Distributed under a Creative Commons Attribution 4.0 International License

Article

Experimental and Theoretical Investigations of Low-Dimensional BiFeO₃ System for Photocatalytic Applications

Manal Benyoussef¹, Sébastien Saitzek² , Nitul S. Rajput³ , Matthieu Courty⁴, Mimoun El Marssi¹ and Mustapha Jouiad^{1,*} 

- ¹ Laboratory of Physics of Condensed Matter (LPMC), University of Picardie Jules Verne, Scientific Pole, 33 Rue Saint-Leu, CEDEX 1, 80039 Amiens, France; manal.benyoussef@u-picardie.fr (M.B.); mimoun.elmarssi@u-picardie.fr (M.E.M.)
- ² Université d'Artois, CNRS, Centrale Lille, ENSCL, Université de Lille, UMR 8181, Unité de Catalyse et Chimie du Solide (UCCS), 62300 Lens, France; sebastien.saitzek@univ-artois.fr
- ³ Advanced Materials Research Center, Technology Innovation Institute, Abu Dhabi P.O. Box 9639, United Arab Emirates; nitul.rajput@tii.ae
- ⁴ Laboratoire de Réactivité et de Chimie des Solides, UMR CNRS 7314, Hub de l'Énergie, Université de Picardie Jules Verne, 80000 Amiens, France; matthieu.courty@u-picardie.fr
- * Correspondence: mustapha.jouiad@u-picardie.fr

Abstract: We report on the fabrication of sub-20 nm BiFeO₃ (BFO) nanoparticles using a solid-state approach and preferential leaching process. The nanoparticles were subsequently used to deposit, through spray pyrolysis, BFO thin films in a rhombohedral (R3c) crystallographic structure. Then, systematic investigations of the optical and the photocatalytic properties were conducted to determine the effects of the particles size, the microstructure and the increased surface area on their catalytic performances. Especially, improved optical properties were observed, with an optical bandgap energy of 2.20 eV compared to reported 2.7 eV for the bulk system. In addition, high optical absorption was obtained in the UV–visible light region reaching up to 90% at 400 nm. The photoelectrochemical measurements revealed a high photocurrent density under visible light irradiation. Besides, density functional theory calculations were performed on both bulk and thin film BFO structures, revealing an interesting comparison of the electronic, magnetic, ferroelectric and optical properties for bulk and thin film BFO systems. Both theoretical and experimental findings show that the alignment of the band edges of BFO thin film is coherent with good photocatalytic water splitting potential, making them desirable photoanode materials.

Keywords: photocatalysis; BiFeO₃ nanoparticles; high energy ball milling; spray pyrolysis; photoelectrochemical measurements; density functional theory



Citation: Benyoussef, M.; Saitzek, S.; Rajput, N.S.; Courty, M.; El Marssi, M.; Jouiad, M. Experimental and Theoretical Investigations of Low-Dimensional BiFeO₃ System for Photocatalytic Applications. *Catalysts* **2022**, *12*, 215. <https://doi.org/10.3390/catal12020215>

Academic Editor: Maria A. Goula

Received: 21 January 2022

Accepted: 9 February 2022

Published: 12 February 2022

Publisher's Note: MDPI stays neutral with regard to jurisdictional claims in published maps and institutional affiliations.



Copyright: © 2022 by the authors. Licensee MDPI, Basel, Switzerland. This article is an open access article distributed under the terms and conditions of the Creative Commons Attribution (CC BY) license (<https://creativecommons.org/licenses/by/4.0/>).

1. Introduction

Energy demand in recent years has shown significant growth owing to the world's growing population and constant development of technology-based industries. Currently, fossil fuels constitute the most dominant energy consumption. Nevertheless, their carbon footprint and harmful gas emissions are at the forefront of environmentally impactful dangers both on peoples' and the globe's health [1,2]. To meet the world's energy needs and support the energy transition to clean and sustainable energy consumption, it is necessary to focus on the development of alternative clean energy resources. Harnessing sunlight energy is perhaps one of the most straightforward and continuously available routes to produce energy on demand clean, sustainable and renewable. Among an important diversity of methods to exploit the solar energy, producing hydrogen through the splitting of water molecules into its constituent elements has recently attracted a lot of interest [3,4]. Nonetheless, a few essential conditions have to be fulfilled in order to produce an efficient Water Splitting (WS) device. The nature of the photocatalyst material is the first and

main component to consider. In this context, several materials have been studied for their photocatalytic activity in the race for the optimal photocatalyst capable of generating a large quantity of hydrogen. Metal oxides were largely investigated as photocatalysts (ex: TiO_2 , SnO_2 , Fe_2O_3 , ZnO) owing to their high stability, efficiency, and especially their low cost [5–8]. Since Fujishima and Honda (1972) brought to light the benefit of TiO_2 single crystal for solar water splitting, many interesting findings were proposed by various researcher groups all over the world [9]. Despite their high potential, the light absorption of metal oxides is limited within the ultra-violet region, which reduces significantly their solar-to-hydrogen (STH) conversion efficiency. Nevertheless, surface modification using plasmonic materials has been reported to significantly enhance the visible light absorption of the photocatalyst [10–14] as well as improving the efficiency of the charge separation and amplification of the electron-hole (e–h) pairs. However, oxidation of the material with the aqueous solution remains a challenging drawback in this case [15].

Recently, perovskite materials (PMs) have emerged as potentially interesting photocatalysts owing to their high electrochemical and photophysical properties [16,17]. The exceptional structural flexibility of PMs allows the design of WS devices with high STH efficiency, thanks to the precise control of the composition, the electronic structure, and the morphology of this class of materials. Particularly, the ferroelectric properties present in PMs were found to promote the photocatalytic activities [18,19]. For instance, the PbTiO_3 compound was reported to have an effective charge separation and good photocatalytic performance which were attributed to its ferroelectric properties [20]. Therefore, owing to their high photocatalytic potential, good stability, structural flexibility, ease of synthesis, and ferroelectric properties, PMs show a high potential for the development of more efficient future water splitting devices. Furthermore, the BFO photocatalyst has already been demonstrated for the degradation of organic compounds such as dyes [21–23], antibiotics [24], and antibacterials [25], as well as a photoanode for hydrogen production [26]. The BFO photocatalytic activity (band gap engineering and restriction of the recombination rate) was also found to be improved by the incorporation of doping agents such as La [27–29], Sm [30], co-catalyst [31], metallic nanoparticles such as gold [32] or silver [33] or by the production of n/p heterojunction [34–36].

This work is focused on the elaboration, characterization and the photocatalytic performances of low-dimensional BFO films deposited by means of spray pyrolysis. Besides, density functional theory is used to investigate the effect of the dimensionality on the optical and photocatalytic properties of the BFO system.

2. Results and Discussion

2.1. Thermal Analysis

Figure 1 presents the thermogravimetric (TGA) and differential scanning calorimetry (DSC) curves of as-milled Bi_2O_3 and Fe_2O_3 mixture in the range of 40 °C to 1100 °C.

As can be seen, the formation of the BFO compound is a complex multi-step reaction process. It is worth noting that the bismuth oxide and the iron oxide are highly hygroscopic oxides prone the moisture uptake in the humid environment. Hence, the first step (40–200 °C) of the weight loss (~1%) could be attributed to the water evaporation along with ethanol solvent used to prepare the BFO powder by the high energy ball milling. At intermediate temperatures, the weight shows abrupt losses about ~2.7% and ~1.5% in the range 200–350 °C, and 350–460 °C, respectively. The first weight loss was reported by Maurya et al. [37] to be induced by the volatilization of bismuth, while the second weight loss is ascribed to the formation of intermediate compounds as reported earlier by Valant et al. [38]. These authors suggested that metallic bismuth compounds could be released, considering the melting point of bismuth oxide is 825 °C. Similar results were reported by Sharma et al. [39] who extensively investigated the formation of bismuth ferrite using a solid-state reaction by TGA/DSC technique. These authors reported that during the synthesis of the BFO compound, the formation of secondary phases, such as $\text{Bi}_2\text{Fe}_4\text{O}_9$ and/or $\text{Bi}_{25}\text{FeO}_{40}$, might occur. Regarding the temperature region from 460 °C to 900 °C, no mass change was noticed, however, the

DSC curve exhibits a large corresponding exothermic peak. This last response is a signature of the temperature of crystallization of the BFO system. Based on the TGA/DSC experiments, a temperature of 700 °C was selected for further BFO powder heat treatment. Furthermore, a strong endothermic peak is observed at 936 °C which could be attributed to the melting point of the BFO compound. The high mass loss observed above 1000 °C is most probably related to Bi_2O_3 evaporation, as previously reported by Palai et al. [40].

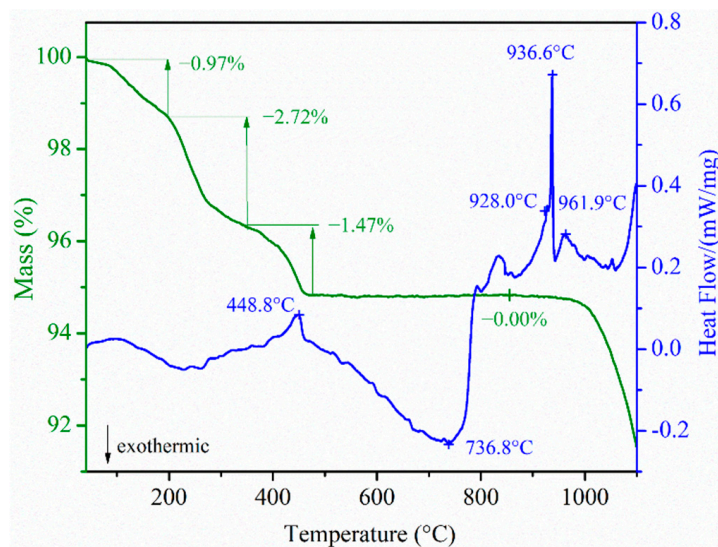


Figure 1. Combined thermogravimetric (TGA) and differential scanning calorimetry (DSC) results obtained on as-milled Bi_2O_3 and Fe_2O_3 mixture.

2.2. X-ray Diffraction

Figure 2 depicts the room temperature X-ray diffractogram of the BFO sample, as fabricated and leached ones at the most relevant diffracting windows for BFO (20° to 60°).

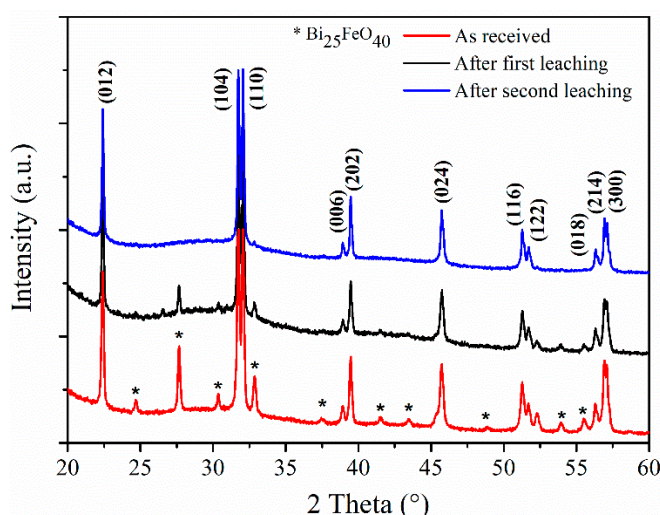


Figure 2. X-ray diffraction patterns of BiFeO_3 compound for (red) as received sample, (black) after the first and (blue) second leaching with acetic acid. (*) indicates $\text{Bi}_{25}\text{FeO}_{40}$ picks positions.

The red plot presents the calcined sample at 700 °C for 1 h. A typical rhombohedral structure is obtained along with a non-negligible secondary phase assigned to the $\text{Bi}_{25}\text{FeO}_{40}$ phase. To remove these impurities, two leaching steps were carried out using glacial acetic acid [41,42]. The second black curve shows the obtained BFO XRD spectra after the first leaching (24 h) which seems to drastically decrease the quantity of undesired phases. To achieve a complete removal of the $\text{Bi}_{25}\text{FeO}_{40}$ secondary phase, a second leaching (48 h)

was done (blue curve), after which no impurity could be detected with a final pure R3c BFO structure. From the XRD pattern of the pure BFO system, we could extract the lattice parameters in the rhombohedral structure with $a = 5.635 \text{ \AA}$, and $\alpha = 59.3918^\circ$.

2.3. Raman Spectroscopy

To further confirm the phase purity of the prepared sample, a micro-Raman (Renishaw) spectrometer was used to examine the vibrational behavior of obtained the BFO structure. The energy excitation used for the analysis is a green laser (532 nm). Figure 3a presents the Raman spectrum of the leached BiFeO_3 sample collected at room temperature from 50 to 550 cm^{-1} .

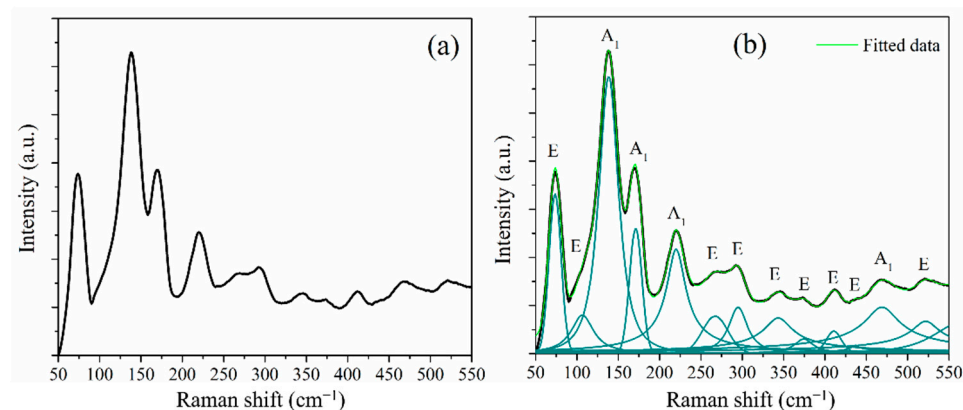


Figure 3. (a) Raman spectrum of BiFeO_3 system. (b) Deconvolution of the Raman spectrum.

The deconvoluted BFO Raman spectrum (Figure 3b) evidences well the presence of the 13 Raman modes, i.e., nine E modes, and four A_1 modes, with the irreducible representation: $\Gamma = 4A_1 + 9E$, of the rhombohedral (R3c) structure of pure BFO system [43–45]. Note that the low-frequency Raman modes, E (1) $\sim 75 \text{ cm}^{-1}$, E (2) $\sim 110 \text{ cm}^{-1}$, A_1 (1) $\sim 138 \text{ cm}^{-1}$, A_1 (2) $\sim 171 \text{ cm}^{-1}$ are assigned to bismuth vibrations and oxygen octahedral tilt in the R3c structure. On the other hand, the middle-frequency Raman modes, A_1 (3), E (3), and E (4) correspond to the vibrations associated to iron atoms [46]. Regarding the high-frequency Raman modes, they are mainly correlated to the motion of oxygen atoms [47–49].

2.4. Microstructure Analysis

After obtaining high purity BFO powders, we investigated the effect of a second stage of a high energy ball milling step of the initial powder. Figure 4 shows the scanning electron microscopy (SEM) images collected of the sprayed BiFeO_3 films with different initially milled powders.

Figure 4a,b presents the BFO sample with no second milling at different magnifications. It can be observed that the surface is not homogenous with regions where grains are aggregated. From Figure 4b, the grain size was observed to vary from 200 to 400 nm. Figure 4c,d presents the sprayed BFO sample from an initial powder with a second 8 h high energy ball milling step. It can be observed that in this case grain size lower than 100 nm was achieved. The obtained results are beneficial to photocatalytic applications owing to the high surface area, high crystallinity confirmed by Raman spectroscopy and free of defects (dislocations), as shown in transmission electron microscopy (TEM) investigations given below. This allows low e-h recombination leading to higher water splitting activity.

TEM investigations were carried out on the BFO nanoparticles obtained after 8 h ball milling and a bright field low magnification micrograph is depicted in the Figure 5a. At this magnification, the particles appear as an aggregate set, while the high-resolution micrographs depicted in Figure 5b,c demonstrate the nanometric scale of the milled particles. The nanoparticle size distribution is extracted and provided in Figure 5d. The crystal size varies from few nm to few tens of nm, with an average size in the range of 5–10 nm.

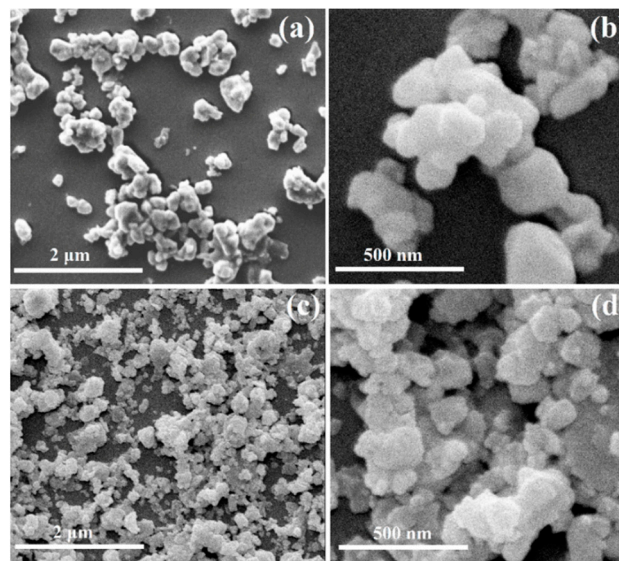


Figure 4. SEM images of the sprayed BiFeO_3 samples on a silicon substrate, with an initial powder with (a,b) no second milling, and (c,d) 8 h of second milling at different magnifications.

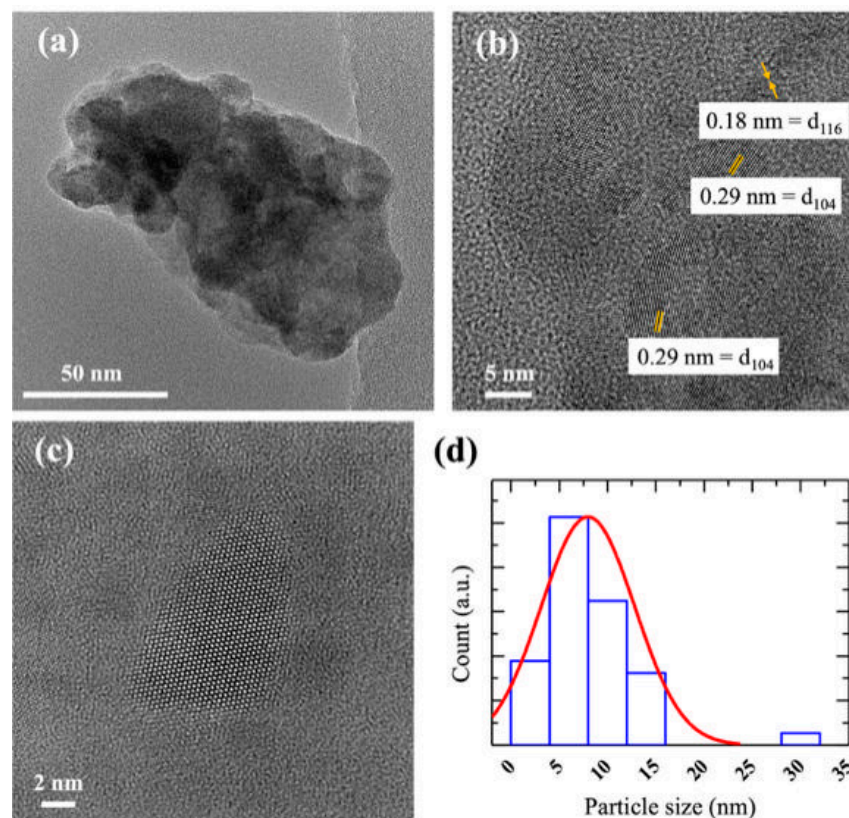


Figure 5. TEM images of the BFO nanoparticles. (a) A bright field TEM image of a set of particles. (b,c) HRTEM images of nanoparticles with different shapes and sizes. (d) The size distribution of the BFO nanoparticles implying the dominant size in the range of 5–10 nm.

2.5. Optical Properties

It should be noted that the absorption in the visible light region of materials is an important parameter to consider for water splitting applications where solar light needs to be mostly absorbed to improve the water splitting efficiency.

Figure 6a presents the absorption, transmittance, and reflectance response of BFO film with no second milling step, where the response of the glass substrate was subtracted.

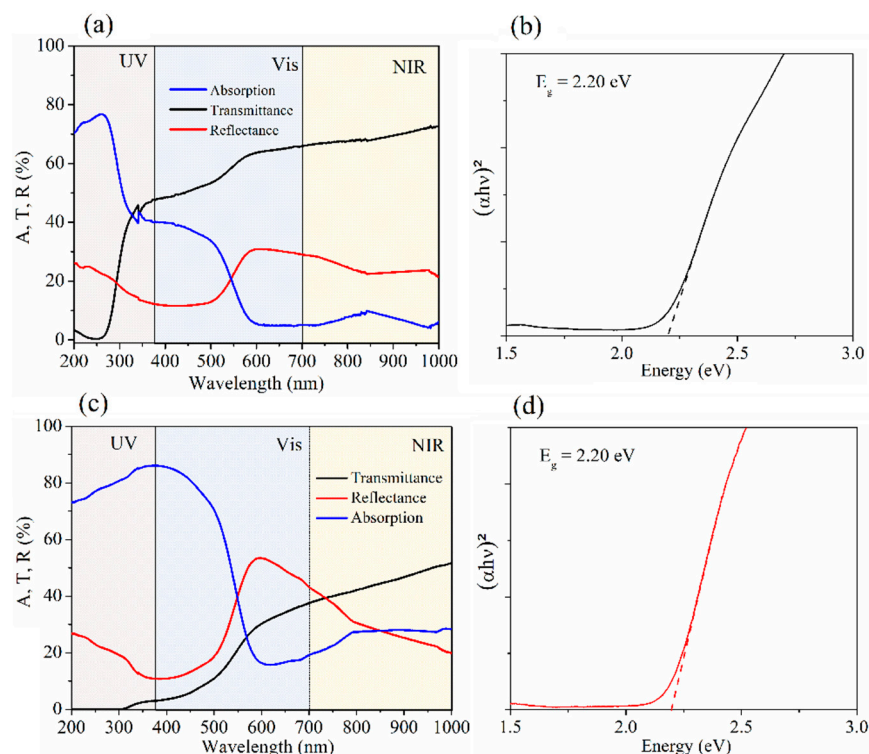


Figure 6. Absorption, transmittance, and reflectance of BiFeO₃ deposited on a glass substrate with (a) no second milling, (c) with 8 h of second milling of the initial powder. Their respective Tauc plots are illustrated in (b,d).

The absorption curve of BFO shows two main peaks, a first dominant response (~75%) in the UV range, and a second one in the visible light region (~40%). The obtained response is very interesting and proves the potential of our prepared films to be good photocatalysts. We also investigated the optical band gap of the sample (shown in Figure 6b) using the Tauc relation: $(\alpha h\nu)^n \propto (h\nu - E_g)$ where $n = 2$ stand for a direct bandgap. Therefore, from the intersection of the extrapolated linear part of $(\alpha h\nu)^2$ versus energy with the energy axis, we could extract the bandgap energy of our sample. A direct band gap energy of 2.20 eV was found for the BFO sample. It is worth mentioning that the usually reported band gap value of the bulk BFO compound is ranging from 2.5 to 2.8 eV [50,51]. Note that Mocherla et al. [52] demonstrated that the bandgap energy value of the BFO system is directly related to the grain size, such that a lower band gap energy can be obtained for samples presenting smaller grain sizes.

Figure 6c presents the absorption, transmittance, and reflectance response of BFO film with a second milling of 8 h. An important increase in the absorption is noticed for wavelengths from 200 to 500 nm, achieving a maximum absorption of ~90% (400 nm). Especially, we can observe an increase in the absorption for wavelengths superior to 600 nm, reaching 15% of absorption at 600 nm instead of 4% for the sample with no second ball milling. The energy band gap of this sample (Figure 6d) was also found to be 2.20 eV.

Therefore, one can say that our original methodology permitted us to achieve high absorption in the UV and visible light region, with a corresponding band gap value of ~2.20 eV, making it an interesting candidate for photocatalysis.

2.6. Photoelectrochemical Measurements

In this section, the potential of the BFO sample for photocurrent generation is examined. Figure 7a present the Mott–Schottky plot $1/C^2(E)$ of BFO film deposited on a Pt/Si

substrate. From the resulting positive slope, we can conclude about an n-type semiconductor type with a flat band potential $E_{fb} = -0.38$ V vs. Ag/AgCl or 0.231 V vs. RHE (at pH = 7). Potentials vs. Ag/AgCl were converted to potentials vs. RHE with following equation [53]:

$$E_{(RHE)} = E_{(Ag/AgCl)} + E_{(Ag/AgCl)}^{\circ} + 0.0591pH \quad (1)$$

where $E_{(Ag/AgCl)}^{\circ}$ (reference electrode, saturated KCl) = 0.197 V vs. NHE at 25 °C.

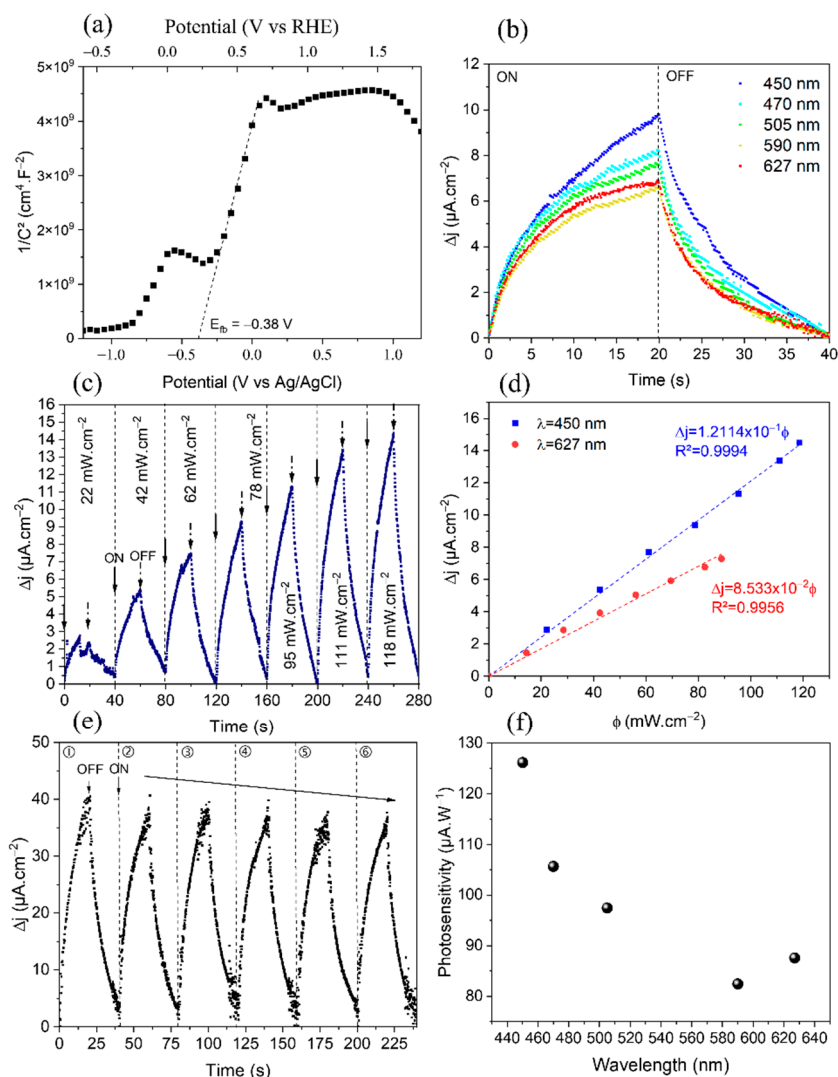


Figure 7. (a) Mott–Schottky plot. (b) Transient photocurrent response under illumination and dark conditions of BFO thin film for various wavelengths ranging from 450 to 627 nm ($\phi = 62$ mW/cm²). (c) Transient photocurrent response (On–Off cycles every 20 s) as a function of the incident light intensity ($\lambda = 450$ nm, and $V = 0.6$ V vs. Ag/AgCl). (d) The evolution of Δj (ϕ) for $\lambda = 450$ and 627 nm and the fit in dashed lines. (e) Transient photocurrent response registered for six cycles ON/OFF (every 20 s) and under constant solar simulator of 100 mW/cm². (f) Photosensitivity of BFO thin film sample as a function of wavelength.

In the depletion zone, a plateau is observed, slightly shifting the flat band potential. This offset may be due to the presence of electrically active defects in the surface (surface states) inducing a Helmholtz layer capacitance as reported [54]. The flat band potential reflects the position of the Fermi level as described [55]. For the n-type semi-conductor, the conduction band (CB) edge is expected to be located very close to 0.1 V of its flat band potential [56]. Therefore, knowing the band gap value, we could locate, respectively,

conduction and valence band edges of processed BFO film at neutral pH at $E_{CB} \sim 0.131$ V vs. NHE, and at $E_{VB} \sim 2.331$ V vs. NHE.

To determine the transient photocurrent, a three-electrode cell, consisting of Ag/AgCl reference electrode, Pt wire as counter electrode, and the working electrode made of BFO film grown on Pt/Si substrate, is used and a solution 0.1 M of Na_2SO_4 is employed as an electrolyte. Figure 7b presents the transient photocurrent response of BFO film under different excitation wavelengths. One can observe the presence of a non-negligible photocurrent for low wavelengths of $\sim 10 \mu\text{A}/\text{cm}^2$ (450 nm) under a light intensity of $\phi = 62 \text{ mW}/\text{cm}^2$ using a bias potential of 0.6 V vs. Ag/AgCl. For the higher excitation wavelengths, the maximum photocurrent decreases but remains significant. For further investigations, in Figure 7c, the photocurrent response (Δj) is measured as a function of the light intensity (ϕ_0 in $\text{mW}\cdot\text{cm}^{-2}$) for constant $\lambda = 450$ nm and $V_{\text{bias}} = 0.6$ V vs. Ag/AgCl.

The dependence of the photocurrent on the incident light intensity (Figure 7c) highlights a linear evolution for BFO films ($\Delta j = A\phi_0$ where A is a wavelength-dependent constant). Indeed, this linear behavior is also observed for other wavelengths (e.g., $\lambda = 627$ nm in Figure 7d). Theoretically, the evolution of the photocurrent as a function of the incident light intensity follows a power law of type $\Delta j = A\phi_0^n$ where A is a wavelength-dependent constant and n a constant (that determines the photosensitivity of the oxide and whose value is less or equal to 1 [57]). In our case, the exponent is equal to 1, which indicates that the process of generating e-h pairs takes place without the influence of trapping phenomena or recombination in unlit areas at this applied bias voltage [58,59]. This result is not surprising because in thin films, thus for small values of the thickness, the illumination is appreciably uniform and Δj varies linearly with ϕ_0 . When thickness increase, the absorption becomes non-uniform in thickness, hence the recombination in the unlit domain increases and the n exponent decreases, its value limit must be 0.5 for very large thicknesses [59].

Figure 7e presents a transient photocurrent response obtained under a solar simulator equivalent to 1 sun ($100 \text{ mW}/\text{cm}^2$, AM 1.5G) and for applied bias voltage of 0.6 V. It is observed the achievement of an important photocurrent density of $40 \mu\text{A}/\text{cm}^2$ within the BFO sample. It is worth noting that the notable photocurrent is generated from as low as an applied voltage of 0.1 V. Besides, a slight decrease of the photocurrent response (see arrow in Figure 7e) is observed, which could be attributed to the degradation of BFO due to the electrolyte. Indeed, BFO contains iron, which is a corrosive material in contact with Na_2SO_4 solution. The obtained photosensitivity ($\mu\text{A}/\text{W}$) of the BFO sample as a function of wavelength (Figure 7f) is in good accordance with the optical measurements presented above. The best efficiency is obtained for low wavelengths, but a photocurrent is produced over the entire visible spectral range. Finally, the position of the valence and conduction bands determined experimentally and the high photocurrent generated in the visible range suggest that the BFO thin film exhibits a great potential to be used as photoanodes within water-splitting photoelectrochemical systems.

2.7. Theoretical Calculations

2.7.1. Electronic Properties

Note that the magnetic properties of the BFO system were considered in our calculations, and both ferromagnetic (FM) and antiferromagnetic (AFM) configurations were studied. It was found that the lowest energy was obtained for the AFM configuration of the BFO system, which agrees well with the literature review [60,61]. In addition, we used two different approximations to ensure the accurate description of the electronic properties of the studied AFM bulk BFO system (Figure 8). We first considered the generalized gradient approximation (GGA) to consider the effect of gradients into the charge density, which is known to improve the calculation of the cohesive energy. From Figure 8, we can observe an extremely low band gap energy of 0.5 eV using the GGA approximation which is still far from the well-known band gap of BFO system (i.e., ~ 2.7 eV) [50,51].

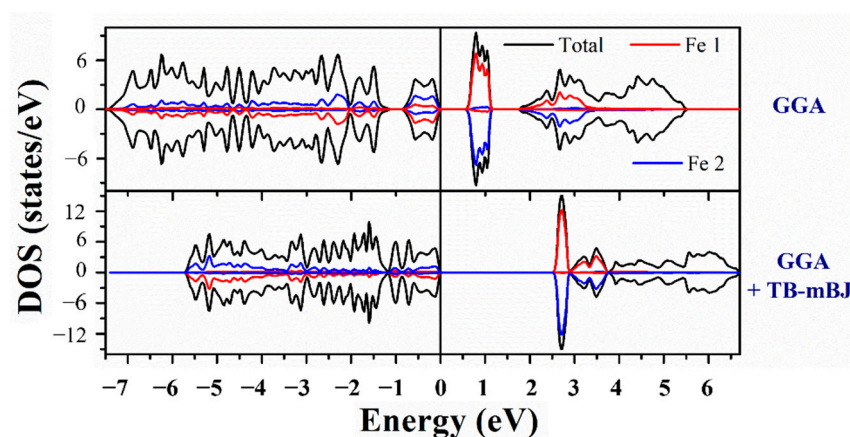


Figure 8. Density of electronic states of the bulk BiFeO₃ compound using three different approximations.

In a view to correct the description of the electronic properties, we implemented our calculations with the Tran and Blaha modified Becke–Johnson (TB-mBJ) exchange potential. The TB-mBJ approximation yields particularly good electronic properties [62], with the achievement of an energy band gap of 2.5 eV, in good accordance with a literature review [63,64].

Figure 9 presents the band structure obtained using the different approximations. Interestingly, it can be seen from the figure that both the nature and the energy of the band gap are different depending on the used approximation. An indirect band gap is observed for the GGA approximation. However, a direct band gap of 2.5 eV can be observed for the GGA + TB-mBJ approximation. Note that several experimental articles reported a direct band gap for BiFeO₃ system [65–67]. Therefore, our calculations permitted us to achieve E_g values closer to the experiment.

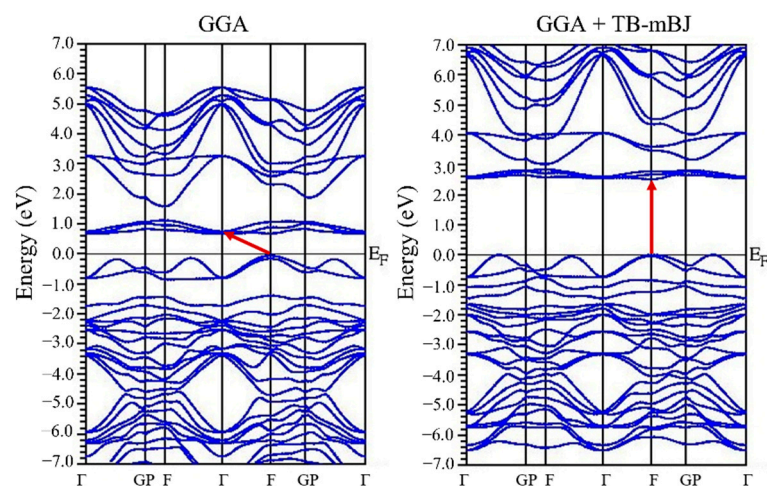


Figure 9. Band structure of BiFeO₃ computed using GGA, and GGA + TB-mBJ.

Figure 10a presents the total and partial density of electronic states of the BiFeO₃ system calculated using the GGA + TB-mBJ approximation. It can be observed from the figure, that owing to the antiferromagnetic ordering considered in our calculations, the spin up and spin down channels are equal with a zero-net total magnetization. Note that both the valence band and the conduction band are constituted of oxygen 2p orbitals, iron 3d, and bismuth 6p orbitals, which reveal the strong Bi–O and Fe–O hybridization. In addition, we can conclude about a strong interaction between bismuth, iron and oxygen atoms, which is confirmed from the electronic density plot presented in Figure 10b. Indeed, Bi and Fe ions are observed to share covalent bonding with oxygen atoms.

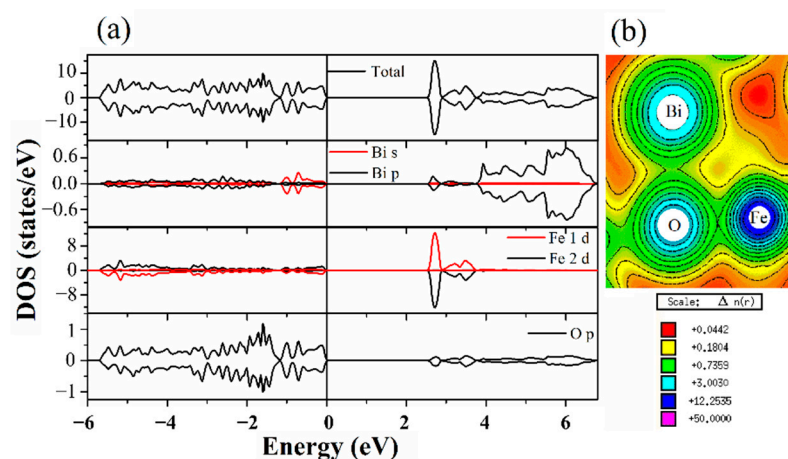


Figure 10. (a) Total and partial density of electronic states, and (b) the charge density distribution (110 plan) of the bulk BiFeO_3 compound.

Since the BFO system, in its rhombohedral structure, is known to present ferroelectric properties, we were also interested in the calculation of the polarization value using the BerryPI approach [68]. Our calculations showed a high polarization value of $83 \mu\text{C}/\text{cm}^2$ in the [111] direction for the bulk AFM BFO system. Note that the high polarization value observed in BFO is in part related to the lone pair effect ($6s^2$) of bismuth atoms [69].

In a view to investigate the effect of dimensionality on BFO system, we also investigated the electronic properties of BiFeO_3 in the thin film form. Figure 11a presents the total and partial density of electronic states of BFO thin film. On the contrary to the bulk system, we can note here that the spin up and spin down channels are not equal even though antiferromagnetic ordering was considered. Fact that resulted in a net non-zero magnetization of $M = 2 \mu_B$ in the BFO thin film. Remind that to simulate thin films we used a 10 \AA vacuum in the z-direction. The induced degree of freedom in the z-direction may have resulted in canted/non-collinear arrangement of spins in the surface. Therefore, the enhanced magnetization in the BFO thin film can be attributed to the canting effect in the surface owing to the uncompensated magnetic moments of iron ions.

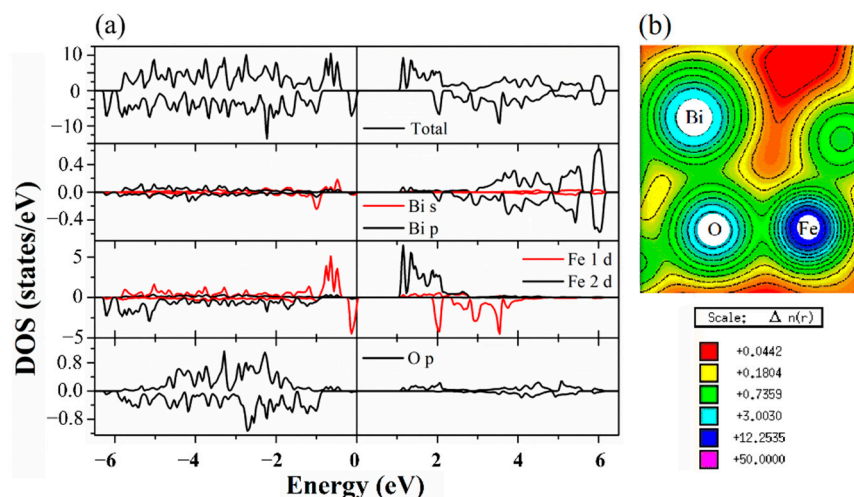


Figure 11. (a) Total and partial density of electronic states, and (b) the charge density distribution (110 plan) of BiFeO_3 in the thin film form.

Indeed, several works reported on the influence of the magnetic field on hydrogen production via water splitting. For instance, Karatza et al. reported a non-negligible hydrogen generation of 0.229 mg from water through a magnetic pre-poling ($M = 48.3 \text{ mT}$) of the Fe_3O_4 system [70]. The magnetic pre-poling was demonstrated to induce re-orientations of

the magnetic poles of each grain making them behave like small magnets and results in the stabilization of the borders between grains [71]. Besides, the presence of both electric and magnetic properties in multiferroic materials permits the manipulation of the magnetism via electric fields and electricity via magnetic fields thanks to the magnetoelectric coupling [72].

Interestingly, the polarization was observed to increase to $93 \mu\text{C}/\text{cm}^2$ for BFO thin films in the [111] direction. The obtained polarization value matches well with reported experimental studies on BFO thin films [73,74]. We plotted in Figure 11b the charge density distribution of BFO thin film, in a view to investigate the origin of the increased ferroelectricity in the system.

Interestingly, a stronger Bi-O and Fe-O bonding (smaller bond length) can be observed in the BFO thin film compared to the bulk one, which can explain the enhanced polarization value obtained in the thin film. Figure 12a,b presents the spin up and spin down parts of the band structure of BiFeO₃ thin film. Note that a direct band gap is observed in both figures with band gap values of 1.6 eV (up) and 2 eV (down). This feature is very interesting and implies that in such system a desired band gap can be promoted using appropriate excitation. In the view to investigate the absorption of the spin up and spin down of BFO system, we plotted in Figure 13a,b the Fe 2p X-ray absorption spectra (XAS), and X-ray magnetic circular dichroism (XMCD) of BiFeO₃ system in both bulk and thin film form.

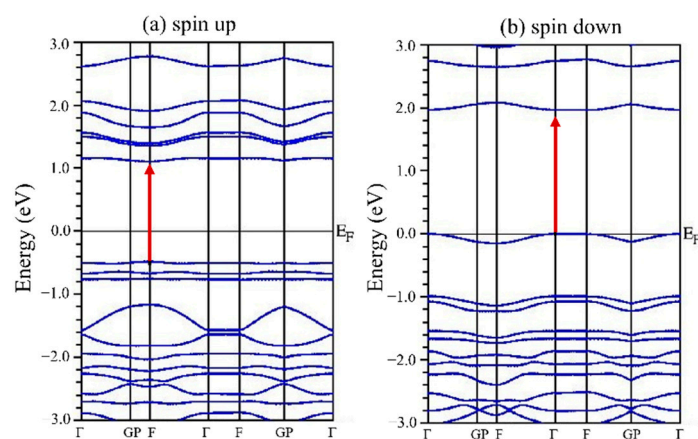


Figure 12. (a) Spin up, and (b) spin down channel of the band structure of BiFeO₃ thin film.

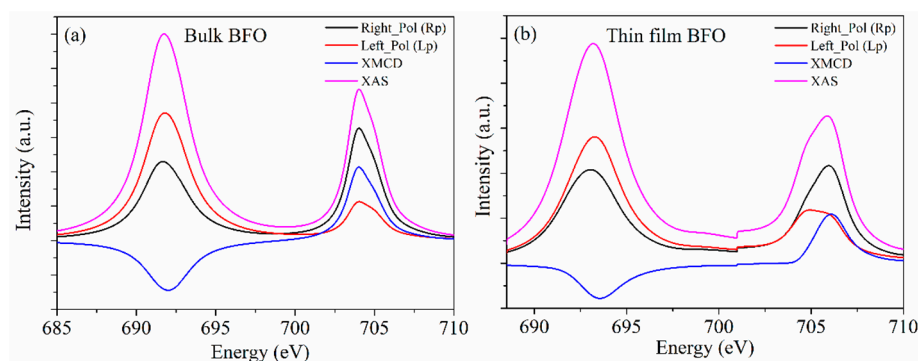


Figure 13. Absorption spectra at the Fe L_{2,3} edges for right circular polarization (RP), left circular polarization (LP) of the exciting X-rays, X-ray magnetic circular dichroism (XMCD) and X-ray absorption spectra (XAS) in the (a) bulk, (b) thin film BiFeO₃ compound.

Regarding the XAS curves, we can observe from the figures two peak responses related to L₃(2p_{3/2}) and L₂(2p_{1/2}) states. The intensity ratio ($I(L_2)/I(L_3)$) of L₂ and L₃ is found to be ~ 0.73 for the bulk and ~ 0.67 for thin film BFO. The decreased intensity ratio indicates an enhanced effect of surface state for the thin film BFO system, as has been reported previously [75,76].

Besides, owing to the octahedral ligand field, the L_2 and L_3 peaks further split to t_{2g} and e_g states. Hence, through the deconvolution of the XAS curves we could extract the crystal-field splitting of the BFO system (i.e., energy difference between t_{2g} and e_g states). A crystal-field value of 1.24 and 1.02 eV was found for BFO thin film, and bulk, respectively, which indicates the presence of a different titanium octahedral environment. In addition, the use of circular polarized light in the X-ray magnetic circular dichroism study makes the absorption signal of the studied element (i.e., iron) sensitive to the magnetic moment. The blue line in Figure 13 illustrates the XMCD signal of Fe $L_{2,3}$ edge which represents the difference value between the left and right circular polarized XAS spectra.

2.7.2. Optical Properties

In this part, we investigated the optical properties of BFO system in its bulk and thin film form using the mBJ approximation. Note that the absorption coefficient, $\alpha(\omega)$, was calculated using the following equation:

$$\alpha(\omega) = \sqrt{2}\omega \sqrt{\sqrt{\varepsilon_1^2(\omega) + \varepsilon_2^2(\omega)} - \varepsilon_1(\omega)} \quad (2)$$

where $\varepsilon_1(\omega)$ and $\varepsilon_2(\omega)$ stand for the real and imaginary parts of the dielectric permittivity, respectively. Figure 14 illustrates the Tauc plots of the BFO system in its bulk and film form, extracted from DFT calculations. It is worth mentioning that in the last years there has been a great number of theoretical investigations reporting on the optical properties of bulk BFO system [77–80]. However, the reported band gap values, as recently demonstrated, are usually misestimated due to the used approximations (e.g., local density and generalized gradient approximations), leading to a truncated description of the strong Coulomb and exchange interactions in transition metal oxides [81]. For instance, using the local spin density approximation (LSDA), Neaton et al. [80] reported an underestimated band gap of 1.9 eV, whereas using the Heyd–Scuseria–Ernzerhof (HSE) screened hybrid functional, Stroppa et al. overestimated the band gap of BFO system to 3.4 eV [79]. In this work, the use of the GGA + TB-mBJ approximation led us to approach quite well the experimental value [50,51], since we have found a direct optical band gap of 2.7 eV for the bulk BFO system (Figure 14a). Indeed, such approximation was previously demonstrated to reproduce rigorously the shape of the exact exchange potential for atoms [82]. In its thin film form, the band gap value of the BFO system was observed to decrease to 2.22 eV (Figure 14b), while keeping the direct band gap nature. Note that it is usually rather difficult to compare the theoretical results (e.g., band gap) of thin films to the experimental ones, since the properties are mainly dependent on various other parameters such as the particle size, morphology, and film thickness [81]. However, in our work the computed band gap value of BFO film appears to be in accordance with the experimental one. The decrease of the band gap in the film form is very interesting for photocatalytic applications, since it presents improved absorption in the visible light region.

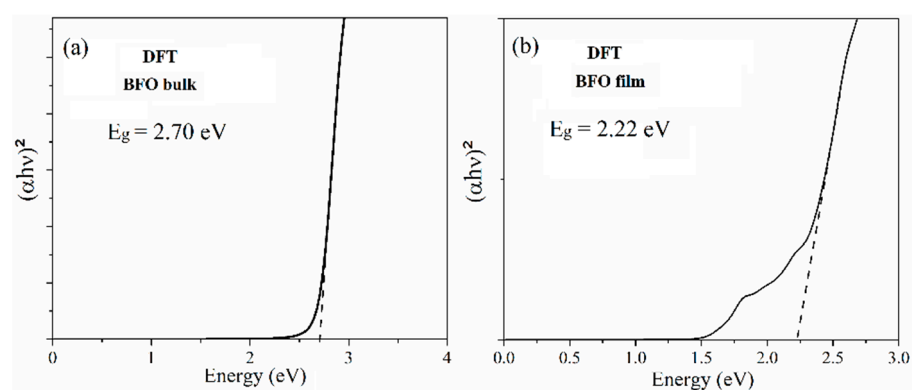


Figure 14. Tauc plot ($n = 2$, direct band gap) of (a) bulk BFO, (b) BFO thin film extracted from DFT.

2.7.3. Photocatalytic Properties

Remember that when a photocatalyst material is irradiated by an energy of incident light higher than its band gap, a charge separation occurs with an electron-hole pair separation causing H_2 and O_2 generation. Hence, the photoexcited electrons in the conduction band (CB) take part in the reduction of water molecules to form H_2 gas ($2H^+ + 2e^- \rightarrow H_2$), whereas the holes in the valence band (VB) are responsible for water oxidation and produce O_2 gas ($H_2O + 2h^+ \rightarrow 2H^+ + \frac{1}{2} O_2$). To efficiently split water molecules, the photocatalyst material should satisfy some basic criteria. First, the material must have a minimum band gap of 1.23 eV ($\lambda = 1000$ nm) to satisfy the redox potential of water. In addition to that, the potential of the top of the valence band (VB) should be higher than the redox potential O_2/H_2O (+1.23 V vs. NHE), and the bottom of the CB should be lower than the redox potential of H^+/H_2 (0 V vs. NHE) [83]. It has been largely reported that the adequate band gap value of the photocatalyst material should be in the range of 1.6–2.4 eV to efficiently satisfy the activation barrier of the multi-step water splitting reactions [83–85]. The conduction band minima, and valence band maxima of our systems (at pH = 0), were computed using Equations (3) and (4), and at specific pH using Equation (5) [86,87]:

$$E_{CB}^{pH=0} = -\frac{1}{2}E_g + \chi_{BFO} + E_0 \quad (3)$$

$$E_{VB}^{pH=0} = +\frac{1}{2}E_g + \chi_{BFO} + E_0 \quad (4)$$

$$E_{(CB,VB)}^{pH} = E_{(CB,VB)}^{pH=0} - 0.05911 \times pH \quad (5)$$

where E_0 represents the scale factor used to link the absolute vacuum scale to the reference redox level ($E_0 = -4.5$ eV) [86], E_g stands for the band gap energy, and χ_{BFO} is the absolute electronegativity of $BiFeO_3$ system. Note that the absolute electronegativity of BFO is given by: $\chi_{BFO} = (\chi_{Bi} \chi_{Fe} \chi_O^3)^{1/5}$, where $\chi_{Bi} = 4.69$, $\chi_{Fe} = 4.06$, and $\chi_O = 7.54$ are the absolute electronegativities of Bi, Fe, and O elements [88].

Figure 15 presents a comparison of the band alignment of BFO thin film computed using Equation (5) and the experimental one extracted from the Mott–Schottky plot at pH = 7. As shown in the figure, both valence and conduction band edges extracted theoretically and experimentally are observed to concord, where E_{VB} is observed to be more positive than the reduction potential of water which allows the occurrence of the oxygen evolution reaction. Our results reveal the potential of reducing dimensionality in the BFO system and should motivate the development of low-dimensional BFO-based films as potential photocatalyst materials and photoanode for water splitting reaction.

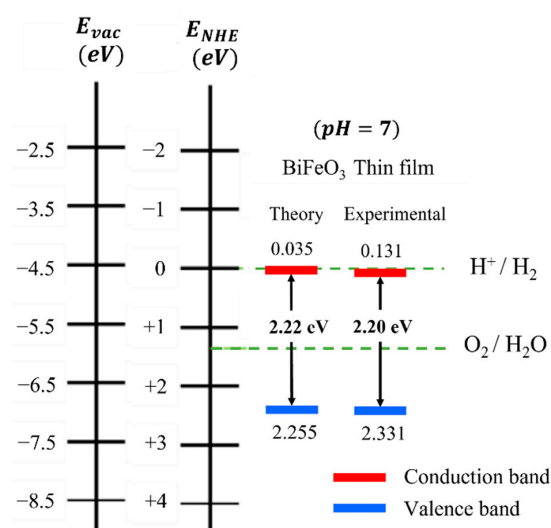


Figure 15. Band alignment of $BiFeO_3$ thin film extracted experimentally and computed theoretically.

3. Materials and Methods

As a first stage, a special focus was given to the elaboration of nanostructured transition metal oxide perovskite BiFeO_3 with controlled grain size through a solid-state synthesis approach by means of the high energy ball milling system. The elaborated BFO powder was used to prepare a solution to be subsequently deposited on glass substrate by means of spray pyrolysis to obtain a neat BFO film. Details of the experimental setup are given in the following paragraph.

First, stoichiometric amounts of bismuth oxide (Bi_2O_3 , 99.99%), and iron oxide (Fe_2O_3 , 99.99%) were weighed and mixed in an ethanol media to be processed by high energy ball milling operating at 1000 rpm for 2 h (Retsch GmbH, Haan, Germany). The high applied rotation speed is expected to achieve BFO powders with small grain size, which would significantly affect the resulting physical properties in comparison with the bulk BFO system. Thereafter, the resulting dried powder was uniaxially pressed into pellets, and placed into a muffle furnace at 700 °C for 1 h at a corresponding cooling/heating rate of 5 °C/min. The resulting pellet was then crushed and pressed in an agate mortar.

The leaching of the powder was performed using glacial acetic acid (99%) to remove the secondary phases. The leached residue was therefore washed with a large volume of distilled water to neutralize the acidity. Both TGA and DSC experiments were performed on the prepared BFO powder using a heating rate of 5 °C/min, in an Argon atmosphere (Netzsch GmbH, Selb, Germany). The phase purity of the resulting powder was investigated using a Bruker X-ray diffractometer (XRD) ($\text{CuK}\alpha = 1.5406 \text{ \AA}$).

A second-high energy ball milling step of 8 h at 1000 rpm was added to the pure powder to investigate the effect of grain size decrease on the physical properties of BFO system. Thence, spray pyrolysis technique was used to subsequently deposit BFO on a desired substrate. A glass substrate was used to characterize the optical properties, whereas a silicon substrate with a sputtered Pt coating was used to investigate the photoelectrochemical properties of BiFeO_3 compound. Before deposition, we first prepared the precursor solution using a molar concentration of 0.1 M in ethanol. Therefore, the solution was stirred in an ultrasonic bath for 1 h until complete dilution. During the deposition process, the prepared BFO solution was pulverized onto the substrate maintained at 400 °C on a hot plate, using compressed air as carrier gas. The duration of the deposition was set to 1 h with a rate of 1 mL/min. The substrate was naturally cooled down to room temperature. The thickness of the deposited BFO film was investigated using a profilometer, and an average thickness of 700 nm was observed. To characterize the microstructure of the deposited film, we used the scanning electron microscope (SEM; Environmental Quanta 200 FEG, Thermo Fisher Scientific, Eindhoven, The Netherlands). Further, transmission electron microscopy (TEM) investigation was done on the BFO nanoparticles to investigate the crystallinity and crystal size of the particles. To prepare the TEM specimen, solution of the BFO powder was prepared and sonicated for 3 min and drop casted on a TEM grid (ultra-thin carbon support film, on lacey carbon) and dried. The TEM experiments were done at 300 kV using an image corrected TEM system (Thermo Fisher Scientific, Titan G2, Eindhoven, The Netherlands). The optical properties were studied using a UV-visible-near IR spectrophotometer in the spectral range of 200–1000 nm operating in both reflective and transmission modes. Note that all the photoelectrochemical investigations were carried on BFO film obtained from the initial powder prepared by the second high energy ball milling process.

The photocurrents and Mott–Schottky plots were collected using an electrochemical device (Autolab PGSTAT204, Metrohm, Herisau, Switzerland) coupled to an LED module (LED Driver kit, Metrohm, Herisau, Switzerland). LEDs (450, 470, 505, 590 and 627 nm) with low spectral dispersion are used. These LEDs are calibrated using a photodiode to determine the density of the luminous flux received by the sample. Three electrodes were used for the measurements, including Ag/AgCl and Pt wire acting as a reference electrode and counter electrode, respectively. The working electrode is made of the thin film with a contact fixed on the platinum layer. This connection is not in contact with the electrolyte

(0.1 M Na₂SO₄ aqueous solution). The Mott–Schottky curves were recorded at 1 kHz and the applied bias voltage was 0.6 V.

The theoretical calculations were performed using the ab-initio self-consistent full-potential linearized augmented plane wave (FLAPW) method based on the density functional theory (DFT), as implemented in the Wien2K code [89]. Besides, we used the modified generalized gradient (GGA) approximation. However, the GGA approach still underestimates the band gap value, therefore we supplement our calculations using the Tran and Blaha modified Beck–Johnson potential (TB-mBJ), which is known to be an accurate approach giving energy bandgaps values closer to the experimental ones [82,90]. The rhombohedral (R3c) structure was used for our calculations. The lattice parameters used for our calculations were directly extracted from the experimental work. Relaxation of the atomic positions was performed to achieve stable structure. Herein, calculations were performed on bulk and thin film BiFeO₃ compounds. Besides, to simulate thin films, we used a vacuum of 10 Å in the z-direction to prohibit periodic conditions.

4. Conclusions

BiFeO₃ nanoparticles were synthesized via a high energy ball milling technique and were subsequently deposited using spray pyrolysis method. BiFeO₃ thin films were found to have a rhombohedral symmetry (R3c). Such good crystallinity was confirmed by X-ray diffraction and TEM investigations. The BiFeO₃ system was found to exhibit 90% of optical absorption in the visible region, which is coherent with the high photocurrent density generated during the photoelectrochemical measurements. The very good catalytic performances achieved, are attributed to the low size of BiFeO₃ (sub-20 nm), which in turn lowers the optical band gap and increases the total surface area. Furthermore, the band alignment edges of BiFeO₃ thin films as demonstrated by both DFT calculations and experimental measurements suggest that low dimensional BiFeO₃ could be used as high performing photoanodes for water splitting reaction.

Author Contributions: Conceptualization, M.B. and M.J.; Investigation, M.B., S.S., M.C., N.S.R., M.E.M. and M.J.; project administration, M.E.M. and M.J.; supervision, M.J.; validation, M.C., S.S., M.E.M. and M.J.; writing original draft, M.B. and M.J.; writing, review and editing, S.S., N.S.R. and M.E.M. All authors have read and agreed to the published version of the manuscript.

Funding: This research was supported by the French Region Haut De France (HDF) (Contract # REG20002).

Data Availability Statement: Data are available from the corresponding author upon request.

Acknowledgments: This research was supported by the French Region HDF “STARS” program. Authors are grateful to the University of Picardie Jules Verne Electron Microscopy facility.

Conflicts of Interest: The authors declare no conflict of interest.

References

1. Nozik, A.J. Photoelectrochemistry: Applications to Solar Energy Conversion. *Annu. Rev. Phys. Chem.* **1978**, *29*, 189–222. [[CrossRef](#)]
2. Nocera, D.G. Personalized Energy: The Home as a Solar Power Station and Solar Gas Station. *ChemSusChem* **2009**, *2*, 387–390. [[CrossRef](#)] [[PubMed](#)]
3. Ni, M.; Leung, M.K.H.; Leung, D.Y.C.; Sumathy, K. A Review and Recent Developments in Photocatalytic Water-Splitting Using TiO₂ for Hydrogen Production. *Renew. Sustain. Energy Rev.* **2007**, *11*, 401–425. [[CrossRef](#)]
4. Moniruddin, M.; Kudaibergenov, S.; Nuraje, N. Hierarchical Nanoheterostructures for Water Splitting. In *Green Photo-Active Nanomaterials: Sustainable Energy and Environmental Remediation*; The Royal Society of Chemistry: London, UK, 2016; Chapter 7; pp. 142–167. ISBN 978-1-84973-959-7.
5. Burda, C.; Lou, Y.; Chen, X.; Samia, A.C.S.; Stout, J.; Gole, J.L. Enhanced Nitrogen Doping in TiO₂ Nanoparticles. *Nano Lett.* **2003**, *3*, 1049–1051. [[CrossRef](#)]
6. Islam, S.Z.; Reed, A.; Wanninayake, N.; Kim, D.Y.; Rankin, S.E. Remarkable Enhancement of Photocatalytic Water Oxidation in N₂/Ar Plasma Treated, Mesoporous TiO₂ Films. *J. Phys. Chem. C* **2016**, *120*, 14069–14081. [[CrossRef](#)]
7. Park, J.H.; Kim, S.; Bard, A.J. Novel Carbon-Doped TiO₂ Nanotube Arrays with High Aspect Ratios for Efficient Solar Water Splitting. *Nano Lett.* **2006**, *6*, 24–28. [[CrossRef](#)]

8. Alexander, F.; AlMheiri, M.; Dahal, P.; Abed, J.; Rajput, N.S.; Aubry, C.; Viegas, J.; Jouiad, M. Water Splitting TiO₂ Composite Material Based on Black Silicon as an Efficient Photocatalyst. *Sol. Energy Mater. Sol. Cells* **2018**, *180*, 236–242. [[CrossRef](#)]
9. Fujishima, A.; Honda, K. Electrochemical Photolysis of Water at a Semiconductor Electrode. *Nature* **1972**, *238*, 37–38. [[CrossRef](#)] [[PubMed](#)]
10. Iwase, A.; Kato, H.; Kudo, A. Nanosized Au Particles as an Efficient Cocatalyst for Photocatalytic Overall Water Splitting. *Catal. Lett.* **2006**, *108*, 7–10. [[CrossRef](#)]
11. Xu, D.; Yang, S.; Jin, Y.; Chen, M.; Fan, W.; Luo, B.; Shi, W. Ag-Decorated ATaO₃ (A = K, Na) Nanocube Plasmonic Photocatalysts with Enhanced Photocatalytic Water-Splitting Properties. *Langmuir* **2015**, *31*, 9694–9699. [[CrossRef](#)] [[PubMed](#)]
12. Abed, J.; Rajput, N.S.; Moutaouakil, A.E.; Jouiad, M. Recent Advances in the Design of Plasmonic Au/TiO₂ Nanostructures for Enhanced Photocatalytic Water Splitting. *Nanomaterials* **2020**, *10*, 2260. [[CrossRef](#)] [[PubMed](#)]
13. Rajput, N.S.; Shao-Horn, Y.; Li, X.-H.; Kim, S.-G.; Jouiad, M. Investigation of Plasmon Resonance in Metal/Dielectric Nanocavities for High-Efficiency Photocatalytic Device. *Phys. Chem. Chem. Phys.* **2017**, *19*, 16989–16999. [[CrossRef](#)]
14. Abed, J.; Alexander, F.; Taha, I.; Rajput, N.; Aubry, C.; Jouiad, M. Investigation of Broadband Surface Plasmon Resonance of Dewetted Au Structures on TiO₂ by Aperture-Probe SNOM and FDTD Simulations. *Plasmonics* **2019**, *14*, 205–218. [[CrossRef](#)]
15. Hu, S.; Lewis, N.S.; Ager, J.W.; Yang, J.; McKone, J.R.; Strandwitz, N.C. Thin-Film Materials for the Protection of Semiconducting Photoelectrodes in Solar-Fuel Generators. *J. Phys. Chem. C* **2015**, *119*, 24201–24228. [[CrossRef](#)]
16. Nuraje, N.; Lei, Y.; Belcher, A. Virus-Templated Visible Spectrum Active Perovskite Photocatalyst. *Catal. Commun.* **2014**, *44*, 68–72. [[CrossRef](#)]
17. Kudo, A.; Miseki, Y. Heterogeneous Photocatalyst Materials for Water Splitting. *Chem. Soc. Rev.* **2009**, *38*, 253–278. [[CrossRef](#)]
18. Grinberg, I.; West, D.V.; Torres, M.; Gou, G.; Stein, D.M.; Wu, L.; Chen, G.; Gallo, E.M.; Akbashev, A.R.; Davies, P.K.; et al. Perovskite Oxides for Visible-Light-Absorbing Ferroelectric and Photovoltaic Materials. *Nature* **2013**, *503*, 509–512. [[CrossRef](#)]
19. Young, S.M.; Rappe, A.M. First Principles Calculation of the Shift Current Photovoltaic Effect in Ferroelectrics. *Phys. Rev. Lett.* **2012**, *109*, 116601. [[CrossRef](#)]
20. Li, H.; Zhu, J.; Wu, Q.; Zhuang, J.; Guo, H.; Ma, Z.; Ye, Y. Enhanced Photovoltaic Properties of PbTiO₃-Based Ferroelectric Thin Films Prepared by a Sol-Gel Process. *Ceram. Int.* **2017**, *43*, 13063–13068. [[CrossRef](#)]
21. Gao, F.; Chen, X.Y.; Yin, K.B.; Dong, S.; Ren, Z.F.; Yuan, F.; Yu, T.; Zou, Z.G.; Liu, J.-M. Visible-Light Photocatalytic Properties of Weak Magnetic BiFeO₃ Nanoparticles. *Adv. Mater.* **2007**, *19*, 2889–2892. [[CrossRef](#)]
22. Soltani, T.; Entezari, M.H. Photolysis and Photocatalysis of Methylene Blue by Ferrite Bismuth Nanoparticles under Sunlight Irradiation. *J. Mol. Catal. A Chem.* **2013**, *377*, 197–203. [[CrossRef](#)]
23. Ponraj, C.; Vinitha, G.; Daniel, J. A Review on the Visible Light Active BiFeO₃ Nanostructures as Suitable Photocatalyst in the Degradation of Different Textile Dyes. *Environ. Nanotechnol. Monit. Manag.* **2017**, *7*, 110–120. [[CrossRef](#)]
24. Mostafaloo, R.; Asadi-Ghalhari, M.; Izanloo, H.; Zayadi, A. Photocatalytic Degradation of Ciprofloxacin Antibiotic from Aqueous Solution by BiFeO₃ Nanocomposites Using Response Surface Methodology. *Glob. J. Environ. Sci. Manag.* **2020**, *6*, 191–202. [[CrossRef](#)]
25. Daub, N.A.; Aziz, F.; Mohd Zain, N.A.; Lau, W.J.; Yusof, N.; Salleh, W.N.W.; Jaafar, J. Photocatalytic Disinfection of Bacteria under Visible Light Irradiation by BiFeO₃ Photocatalyst. *IOP Conf. Ser. Mater. Sci. Eng.* **2021**, *1142*, 012002. [[CrossRef](#)]
26. Deng, J.; Banerjee, S.; Mohapatra, S.K.; Smith, Y.R.; Misra, M. Bismuth Iron Oxide Nanoparticles as Photocatalyst for Solar Hydrogen Generation from Water. *J. Fundam. Renew. Energy Appl.* **2011**, *1*. [[CrossRef](#)]
27. Lan, S.; Yu, C.; Sun, F.; Chen, Y.; Chen, D.; Mai, W.; Zhu, M. Tuning Piezoelectric Driven Photocatalysis by La-Doped Magnetic BiFeO₃-Based Multiferroics for Water Purification. *Nano Energy* **2022**, *93*, 106792. [[CrossRef](#)]
28. Nkwachukwu, O.V.; Muzenda, C.; Ojo, B.O.; Zwane, B.N.; Koiki, B.A.; Orimolade, B.O.; Nkosi, D.; Mabuba, N.; Arotiba, O.A. Photoelectrochemical Degradation of Organic Pollutants on a La³⁺ Doped BiFeO₃ Perovskite. *Catalysts* **2021**, *11*, 1069. [[CrossRef](#)]
29. Dhanalakshmi, R.; Muneeswaran, M.; Shalini, K.; Giridharan, N.V. Enhanced Photocatalytic Activity of La-Substituted BiFeO₃ Nanostructures on the Degradation of Phenol Red. *Mater. Lett.* **2016**, *165*, 205–209. [[CrossRef](#)]
30. Hu, Z.; Chen, D.; Wang, S.; Zhang, N.; Qin, L.; Huang, Y. Facile Synthesis of Sm-Doped BiFeO₃ Nanoparticles for Enhanced Visible Light Photocatalytic Performance. *Mater. Sci. Eng. B* **2017**, *220*, 1–12. [[CrossRef](#)]
31. Xiao, S.; Fakhri, A.; Janani, B.J. Synthesis of Spinel Tin Ferrite Decorated on Bismuth Ferrite Nanostructures for Synergetic Photocatalytic, Superior Drug Delivery, and Antibacterial Efficiencies. *Surf. Interfaces* **2021**, *27*, 101490. [[CrossRef](#)]
32. Bera, S.; Ghosh, S.; Shyamal, S.; Bhattacharya, C.; Basu, R.N. Photocatalytic Hydrogen Generation Using Gold Decorated BiFeO₃ Heterostructures as an Efficient Catalyst under Visible Light Irradiation. *Sol. Energy Mater. Sol. Cells* **2019**, *194*, 195–206. [[CrossRef](#)]
33. Jaffari, Z.H.; Lam, S.-M.; Sin, J.-C.; Zeng, H. Boosting Visible Light Photocatalytic and Antibacterial Performance by Decoration of Silver on Magnetic Spindle-like Bismuth Ferrite. *Mater. Sci. Semicond. Process.* **2019**, *101*, 103–115. [[CrossRef](#)]
34. Niu, F.; Chen, D.; Qin, L.; Zhang, N.; Wang, J.; Chen, Z.; Huang, Y. Facile Synthesis of Highly Efficient p–n Heterojunction CuO/BiFeO₃ Composite Photocatalysts with Enhanced Visible-Light Photocatalytic Activity. *ChemCatChem* **2015**, *7*, 3279–3289. [[CrossRef](#)]
35. Bargozideh, S.; Tasvir, M.; Shekarabi, S.; Daneshgar, H. Magnetic BiFeO₃ Decorated UiO-66 as a p–n Heterojunction Photocatalyst for Simultaneous Degradation of a Binary Mixture of Anionic and Cationic Dyes. *New J. Chem.* **2020**, *44*, 13083–13092. [[CrossRef](#)]

36. Duan, F.; Ma, Y.; Lv, P.; Sheng, J.; Lu, S.; Zhu, H.; Du, M.; Chen, X.; Chen, M. Oxygen Vacancy-Enriched Bi₂O₃/BiFeO₃ p-n Heterojunction Nanofibers with Highly Efficient Photocatalytic Activity under Visible Light Irradiation. *Appl. Surf. Sci.* **2021**, *562*, 150171. [[CrossRef](#)]
37. Maurya, D.; Thota, H.; Nalwa, K.S.; Garg, A. BiFeO₃ Ceramics Synthesized by Mechanical Activation Assisted versus Conventional Solid-State-Reaction Process: A Comparative Study. *J. Alloys Compd.* **2009**, *477*, 780–784. [[CrossRef](#)]
38. Valant, M.; Axelsson, A.-K.; Alford, N. Peculiarities of a Solid-State Synthesis of Multiferroic Polycrystalline BiFeO₃. *Chem. Mater.* **2007**, *19*, 5431–5436. [[CrossRef](#)]
39. Sharma, P.; Diwan, P.K.; Pandey, O.P. Impact of Environment on the Kinetics Involved in the Solid-State Synthesis of Bismuth Ferrite. *Mater. Chem. Phys.* **2019**, *233*, 171–179. [[CrossRef](#)]
40. Palai, R.; Katiyar, R.S.; Schmid, H.; Tissot, P.; Clark, S.J.; Robertson, J.; Redfern, S.A.T.; Catalan, G.; Scott, J.F. β Phase and γ - β Metal-Insulator Transition in Multiferroic BiFeO₃. *Phys. Rev. B* **2008**, *77*, 14110. [[CrossRef](#)]
41. Hasan, M.; Islam, M.D.F.; Mahbub, R.; Hossain, M.D.S.; Hakim, M.A. A Soft Chemical Route to the Synthesis of BiFeO₃ Nanoparticles with Enhanced Magnetization. *Mater. Res. Bull.* **2016**, *73*, 179–186. [[CrossRef](#)]
42. Achenbach, G.D.; James, W.J.; Gerson, R. Preparation of Single-Phase Polycrystalline BiFeO₃. *J. Am. Ceram. Soc.* **1967**, *50*, 437. [[CrossRef](#)]
43. Hlinka, J.; Pokorný, J.; Karimi, S.; Reaney, I.M. Angular Dispersion of Oblique Phonon Modes in BiFeO₃ from Micro-Raman Scattering. *Phys. Rev. B* **2011**, *83*, 20101. [[CrossRef](#)]
44. Hermet, P.; Goffinet, M.; Kreisel, J.; Ghosez, P.H. Raman and Infrared Spectra of Multiferroic Bismuth Ferrite from First Principles. *Phys. Rev. B* **2007**, *75*, 220102. [[CrossRef](#)]
45. Bielecki, J.; Svedlindh, P.; Tibebu, D.T.; Cai, S.; Eriksson, S.-G.; Börjesson, L.; Knee, C.S. Structural and Magnetic Properties of Isovalently Substituted Multiferroic BiFeO₃: Insights from Raman Spectroscopy. *Phys. Rev. B* **2012**, *86*, 184422. [[CrossRef](#)]
46. Sinha, K.; Mascarenhas, A.; Horner, G.S.; Bertness, K.A.; Kurtz, S.R.; Olson, J.M. Raman Line-Shape Analysis of Random and Spontaneously Ordered GaInP₂ Alloy. *Phys. Rev. B* **1994**, *50*, 7509–7513. [[CrossRef](#)]
47. Belhadi, J.; Yousfi, S.; Bouyanfif, H.; El Marssi, M. Structural Investigation of (111) Oriented (BiFeO₃)_(1-x) Λ /(LaFeO₃)_x Λ Superlattices by X-Ray Diffraction and Raman Spectroscopy. *J. Appl. Phys.* **2018**, *123*, 154103. [[CrossRef](#)]
48. Fukumura, H.; Harima, H.; Kisoda, K.; Tamada, M.; Noguchi, Y.; Miyayama, M. Raman Scattering Study of Multiferroic BiFeO₃ Single Crystal. *J. Magn. Magn. Mater.* **2007**, *310*, e367–e369. [[CrossRef](#)]
49. Chang, L.-Y.; Tu, C.-S.; Chen, P.-Y.; Chen, C.-S.; Schmidt, V.H.; Wei, H.-H.; Huang, D.-J.; Chan, T.-S. Raman Vibrations and Photovoltaic Conversion in Rare Earth Doped (Bi_{0.93}RE_{0.07})FeO₃ (RE=Dy, Gd, Eu, Sm) Ceramics. *Ceram. Int.* **2016**, *42*, 834–842. [[CrossRef](#)]
50. Ramachandran, B.; Dixit, A.; Naik, R.; Lawes, G.; Rao, M.S.R. Charge Transfer and Electronic Transitions in Polycrystalline BiFeO₃. *Phys. Rev. B* **2010**, *82*, 12102. [[CrossRef](#)]
51. Catalan, G.; Scott, J.F. Physics and Applications of Bismuth Ferrite. *Adv. Mater.* **2009**, *21*, 2463–2485. [[CrossRef](#)]
52. Mocherla, P.S.V.; Karthik, C.; Ubig, R.; Ramachandra Rao, M.S.; Sudakar, C. Tunable Bandgap in BiFeO₃ Nanoparticles: The Role of Microstrain and Oxygen Defects. *Appl. Phys. Lett.* **2013**, *103*, 22910. [[CrossRef](#)]
53. Radmilovic, A.; Smart, T.J.; Ping, Y.; Choi, K.-S. Combined Experimental and Theoretical Investigations of N-Type BiFeO₃ for Use as a Photoanode in a Photoelectrochemical Cell. *Chem. Mater.* **2020**, *32*, 3262–3270. [[CrossRef](#)]
54. Uosaki, K.; Kita, H. Effects of the Helmholtz Layer Capacitance on the Potential Distribution at Semiconductor/Electrolyte Interface and the Linearity of the Mott-Schottky Plot. *J. Electrochem. Soc.* **1983**, *130*, 895–897. [[CrossRef](#)]
55. Basic Theories of Semiconductor Electrochemistry. In *Electrochemistry of Silicon and Its Oxide*; Zhang, X.G. (Ed.) Springer: Boston, MA, USA, 2001; pp. 1–43. ISBN 978-0-306-47921-2.
56. Kalanur, S.S. Structural, Optical, Band Edge and Enhanced Photoelectrochemical Water Splitting Properties of Tin-Doped WO₃. *Catalysts* **2019**, *9*, 456. [[CrossRef](#)]
57. Huang, S.-M.; Huang, S.-J.; Yan, Y.-J.; Yu, S.-H.; Chou, M.; Yang, H.-W.; Chang, Y.-S.; Chen, R.-S. Highly Responsive Photoconductance in a Sb₂SeTe₂ Topological Insulator Nanosheet at Room Temperature. *RSC Adv.* **2017**, *7*, 39057–39062. [[CrossRef](#)]
58. Zheng, K.; Luo, L.-B.; Zhang, T.-F.; Liu, Y.-H.; Yu, Y.-Q.; Lu, R.; Qiu, H.-L.; Li, Z.-J.; Andrew Huang, J.C. Optoelectronic Characteristics of a near Infrared Light Photodetector Based on a Topological Insulator Sb₂Te₃ Film. *J. Mater. Chem. C* **2015**, *3*, 9154–9160. [[CrossRef](#)]
59. Carles, D.; Lefrançois, G.; Vautier, C. Influence de l'intensité lumineuse sur la photoconduction des couches de selenium amorphe. *Le J. De Phys. Colloq.* **1982**, *43*, C9-327–C9-330. [[CrossRef](#)]
60. Diéguez, O.; González-Vázquez, O.E.; Wojdeł, J.C.; Íñiguez, J. First-Principles Predictions of Low-Energy Phases of Multiferroic BiFeO₃. *Phys. Rev. B* **2011**, *83*, 94105. [[CrossRef](#)]
61. Hatt, A.J.; Spaldin, N.A.; Ederer, C. Strain-Induced Isosymmetric Phase Transition in BiFeO₃. *Phys. Rev. B* **2010**, *81*, 54109. [[CrossRef](#)]
62. Koller, D.; Tran, F.; Blaha, P. Merits and Limits of the Modified Becke-Johnson Exchange Potential. *Phys. Rev. B* **2011**, *83*, 195134. [[CrossRef](#)]
63. Ihlefeld, J.F.; Podraza, N.J.; Liu, Z.K.; Rai, R.C.; Xu, X.; Heeg, T.; Chen, Y.B.; Li, J.; Collins, R.W.; Musfeldt, J.L.; et al. Optical Band Gap of BiFeO₃ Grown by Molecular-Beam Epitaxy. *Appl. Phys. Lett.* **2008**, *92*, 142908. [[CrossRef](#)]

64. Moubah, R.; Schmerber, G.; Rousseau, O.; Colson, D.; Viret, M. Photoluminescence Investigation of Defects and Optical Band Gap in Multiferroic BiFeO₃ Single Crystals. *Appl. Phys. Express* **2012**, *5*, 035802. [[CrossRef](#)]
65. Sando, D.; Carrétéro, C.; Grisolia, M.N.; Barthélémy, A.; Nagarajan, V.; Bibes, M. Revisiting the Optical Band Gap in Epitaxial BiFeO₃ Thin Films. *Adv. Opt. Mater.* **2018**, *6*, 1700836. [[CrossRef](#)]
66. Khan, H.A.A.; Ullah, S.; Rehman, G.; Khan, S.; Ahmad, I. First Principle Study of Band Gap Nature, Spontaneous Polarization, Hyperfine Field and Electric Field Gradient of Desirable Multiferroic Bismuth Ferrite (BiFeO₃). *J. Phys. Chem. Solids* **2021**, *148*, 109737. [[CrossRef](#)]
67. Hasan, M.; Basith, M.A.; Zubair, M.A.; Hossain, M.D.S.; Mahbub, R.; Hakim, M.A.; Islam, M.D.F. Saturation Magnetization and Band Gap Tuning in BiFeO₃ Nanoparticles via Co-Substitution of Gd and Mn. *J. Alloys Compd.* **2016**, *687*, 701–706. [[CrossRef](#)]
68. Ahmed, S.J.; Kivinen, J.; Zaporzan, B.; Curiel, L.; Pichardo, S.; Rubel, O. BerryPI: A Software for Studying Polarization of Crystalline Solids with WIEN2k Density Functional All-Electron Package. *Comput. Phys. Commun.* **2013**, *184*, 647–651. [[CrossRef](#)]
69. Yang, F.; Li, M.; Li, L.; Wu, P.; Pradal-Velázquez, E.; Sinclair, D.C. Defect chemistry and electrical properties of sodium bismuth titanate perovskite. *J. Mater. Chem. A* **2018**, *6*, 5243–5254. [[CrossRef](#)]
70. Karatza, D.; Konstantopoulos, C.; Chianese, S.; Diplas, S.; Svec, P.; Hristoforou, E.; Musmarra, D. Hydrogen Production through Water Splitting at Low Temperature over Fe₃O₄ Pellet: Effects of Electric Power, Magnetic Field, and Temperature. *Fuel Process. Technol.* **2021**, *211*, 106606. [[CrossRef](#)]
71. Changsheng, L.; Hao, W.; Tao, Z. Hard Magnetization Direction and Its Relation with Permeability of Conventional Grain-Oriented Electrical Steel. *Rare Met. Mater. Eng.* **2016**, *45*, 1369–1373. [[CrossRef](#)]
72. Kuzmenko, A.M.; Szaller, D.; Kain, T.H.; Dzion, V.; Weymann, L.; Shuvaev, A.; Pimenov, A.; Mukhin, A.A.; Ivanov, V.Y.; Gudim, I.A.; et al. Switching of Magnons by Electric and Magnetic Fields in Multiferroic Borates. *Phys. Rev. Lett.* **2018**, *120*, 27203. [[CrossRef](#)]
73. H'Mök, H.; Martínez Aguilar, E.; Antúnez García, J.; Ribas Ariño, J.; Mestres, L.; Alemany, P.; Galván, D.H.; Siqueiros Beltrones, J.M.; Raymond Herrera, O. Theoretical Justification of Stable Ferromagnetism in Ferroelectric BiFeO₃ by First-Principles. *Comput. Mater. Sci.* **2019**, *164*, 66–73. [[CrossRef](#)]
74. Belhadi, J.; Ruvalcaba, J.; Yousfi, S.; el Marssi, M.; Cordova, T.; Matzen, S.; Lecoeur, P.; Bouyanfif, H. Conduction Mechanism and Switchable Photovoltaic Effect in (1 1 1) Oriented BiFe_{0.95}Mn_{0.05}O₃ Thin Film. *J. Phys. Condens. Matter* **2019**, *31*, 275701. [[CrossRef](#)] [[PubMed](#)]
75. Higuchi, T.; Liu, Y.-S.; Yao, P.; Glans, P.-A.; Guo, J.; Chang, C.; Wu, Z.; Sakamoto, W.; Itoh, N.; Shimura, T.; et al. Electronic Structure of Multiferroic BiFeO₃ by Resonant Soft X-ray Emission Spectroscopy. *Phys. Rev. B* **2008**, *78*, 85106. [[CrossRef](#)]
76. Béa, H.; Bibes, M.; Fusil, S.; Bouzehouane, K.; Jacquet, E.; Rode, K.; Bencok, P.; Barthélémy, A. Investigation on the Origin of the Magnetic Moment of BiFeO₃ Thin Films by Advanced X-ray Characterizations. *Phys. Rev. B* **2006**, *74*, 20101. [[CrossRef](#)]
77. Bilk, D.I.; Orlando, R.; Shaltaf, R.; Rignanese, G.-M.; Íñiguez, J.; Ghosez, P.H. Hybrid Exchange-Correlation Functional for Accurate Prediction of the Electronic and Structural Properties of Ferroelectric Oxides. *Phys. Rev. B* **2008**, *77*, 165107. [[CrossRef](#)]
78. Clark, S.J.; Robertson, J. Energy Levels of Oxygen Vacancies in BiFeO₃ by Screened Exchange. *Appl. Phys. Lett.* **2009**, *94*, 022902. [[CrossRef](#)]
79. Stroppa, A.; Picozzi, S. Hybrid Functional Study of Proper and Improper Multiferroics. *Phys. Chem. Chem. Phys.* **2010**, *12*, 5405–5416. [[CrossRef](#)]
80. Neaton, J.B.; Ederer, C.; Waghmare, U.V.; Spaldin, N.A.; Rabe, K.M. First-Principles Study of Spontaneous Polarization in Multiferroic BiFeO₃. *Phys. Rev. B* **2005**, *71*, 14113. [[CrossRef](#)]
81. McDonnell, K.A.; Wadnerkar, N.; English, N.J.; Rahman, M.; Dowling, D. Photo-Active and Optical Properties of Bismuth Ferrite (BiFeO₃): An Experimental and Theoretical Study. *Chem. Phys. Lett.* **2013**, *572*, 78–84. [[CrossRef](#)]
82. Tran, F.; Blaha, P.; Schwarz, K. Band Gap Calculations with Becke–Johnson Exchange Potential. *J. Phys. Condens. Matter* **2007**, *19*, 196208. [[CrossRef](#)]
83. Ismail, A.A.; Bahnemann, D.W. Photochemical Splitting of Water for Hydrogen Production by Photocatalysis: A Review. *Sol. Energy Mater. Sol. Cells* **2014**, *128*, 85–101. [[CrossRef](#)]
84. Kim, J.H.; Hansora, D.; Sharma, P.; Jang, J.W.; Lee, J.S. Toward Practical Solar Hydrogen Production—an Artificial Photosynthetic Leaf-to-Farm Challenge. *Chem. Soc. Rev.* **2019**, *48*, 1908–1971. [[CrossRef](#)]
85. Chen, S.; Takata, T.; Domen, K. Particulate Photocatalysts for Overall Water Splitting. *Nat. Rev. Mater.* **2017**, *2*, 17050. [[CrossRef](#)]
86. Zhang, C.; Jiang, N.; Xu, S.; Li, Z.; Liu, X.; Cheng, T.; Han, A.; Lv, H.; Sun, W.; Hou, Y. Towards High Visible Light Photocatalytic Activity in Rare Earth and N Co-Doped SrTiO₃: A First Principles Evaluation and Prediction. *RSC Adv.* **2017**, *7*, 16282–16289. [[CrossRef](#)]
87. Wang, G.-Z.; Chen, H.; Luo, X.-K.; Yuan, H.-K.; Kuang, A.-L. Bandgap Engineering of SrTiO₃/NaTaO₃ Heterojunction for Visible Light Photocatalysis. *Int. J. Quantum Chem.* **2017**, *117*, e25424. [[CrossRef](#)]
88. Pearson, R.G. Absolute Electronegativity and Hardness: Application to Inorganic Chemistry. *Inorg. Chem.* **1988**, *27*, 734–740. [[CrossRef](#)]
89. Schwarz, K.; Blaha, P.; Madsen, G.K.H. Electronic Structure Calculations of Solids Using the WIEN2k Package for Material Sciences. *Comput. Phys. Commun.* **2002**, *147*, 71–76. [[CrossRef](#)]
90. Tran, F.; Blaha, P. Accurate Band Gaps of Semiconductors and Insulators with a Semilocal Exchange-Correlation Potential. *Phys. Rev. Lett.* **2009**, *102*, 226401. [[CrossRef](#)]